Frequency splittings in deformed optical microdisk cavities

Chang-Hwan Yi,[1,*] Julius Kullig,[1] Chil-Min Kim,[2] and Jan Wiersig[1]
[1]*Institut für Theoretische Physik, Otto-von-Guericke-Universität Magdeburg, Postfach 4120, D-39016 Magdeburg, Germany*
[2]*Department of Emerging Materials Science, DGIST, Daegu 711-873, Korea*
(Received 3 July 2017; published 22 August 2017)

We study the frequency splitting of nearly degenerate optical modes in weakly deformed microdisks. The analysis is restricted to even- and odd-parity modes in cavities with a mirror-reflection symmetry. The frequency splitting is explained in a semiclassical approach by dynamical tunneling (resonance-assisted tunneling) between clockwise- and counterclockwise-propagating waves. We derive semiclassical predictions for the frequency splittings which are in good agreement with full numerical calculations. Two deformations are studied in detail, the ellipse and the quadrupole, representing a deformation with integrable and nonintegrable ray dynamics. Furthermore, the differences between Dirichlet and dielectric boundary conditions are discussed.

DOI: 10.1103/PhysRevA.96.023848

I. INTRODUCTION

Dynamical tunneling is a generalization of conventional tunneling which connects classically disjoint regions in phase space [1–9]. Special attention has been paid to resonance-assisted tunneling (RAT) [10–13] across nonlinear resonance chains and chaos-assisted tunneling [14–16] across chaotic regions of phase space. There have been a lot of experimental efforts to study and exploit dynamical tunneling in various kinds of systems such as quantum-dot [17,18], microdisk-cavity [19–23], microwave [24–27], and cold-atom [28] systems.

Optical microcavities have attracted considerable interest in the recent decades [29]. Among the various possible geometries, deformed microcavities have been studied in detail as they serve as model systems for wave chaos and non-Hermitian physics [30]. One obvious effect of a deformation is the splitting of frequencies of mode pairs. This has been experimentally observed in a microdisk cavity [31] and in micropillar cavities [32–35]. In the latter case it was proposed to exploit the splitting for polarization control [32]. In these studies the deformation was assumed to be elliptical even though strong deviations from the ellipse can be identified, e.g., in Ref. [31].

The aim of this paper is to quantify the role of the deformation in the case of microdisk cavities. We show that the frequency splittings can be calculated semiclassically in terms of RAT. As representative models, the elliptic and quadrupole cavities for integrable and nonintegrable deformations are considered. The importance of the dielectric boundary conditions is discussed in detail.

This paper is organized as follows. In Sec. II we introduce the two different cavity shapes and explain how we compare their degree of deformation. Section III obtains the frequency splittings in the elliptic and the quadrupole cavity using full numerics. Section IV discusses the ray dynamical phase space. In Sec. V, we introduce the pendulum approximation for RAT. Section VI derives frequency splittings based on the most prominent resonance chain. Section VII computes the modifications of the frequency splittings resulting from additional resonance chains. Section VIII contains a summary.

*changhwan.yi@ovgu.de

II. THE CAVITY SHAPES

The elliptic shape is expressed in Cartesian coordinates

$$\frac{x^2}{a^2}+\frac{y^2}{b^2}=1, \tag{1}$$

where a and b are the major and minor axes of the ellipse, respectively. By defining $a/R \equiv 1/\sqrt[4]{1-\varepsilon^2}$ and $b/R \equiv \sqrt[4]{1-\varepsilon^2}$, we fix the area of the ellipse (divided by R^2) to be $\pi ab/R^2=\pi$, which is independent of the eccentricity ε. R is the radius of the circle in the limit $\varepsilon \to 0$.

The quadrupole [36] is expressed in polar coordinates

$$\rho_q(\phi;\mu)=\mathcal{R}(\mu)(1+\mu\cos 2\phi) \tag{2}$$

with parameter μ and normalizing factor $\mathcal{R}(\mu) \equiv R/\sqrt{1+\mu^2/2}$. The latter is introduced in order to fix the area (divided by R^2) to be also π.

For a fair comparison of ellipse and quadrupole, we follow Ref. [37] and write the boundary of the ellipse in polar coordinates:

$$\rho_e(\phi;\varepsilon)=R\frac{\sqrt[4]{1-\varepsilon^2}}{\sqrt{1-\varepsilon^2\cos^2\phi}}. \tag{3}$$

For small deformation $\varepsilon \ll 1$ this can be expanded into

$$\rho_e(\phi;\mu)/R \approx 1+\mu\cos 2\phi+O(\mu^2) \tag{4}$$

with the identification

$$\mu(\varepsilon) \equiv 1-\sqrt[4]{1-\varepsilon^2}. \tag{5}$$

Equation (4) is of the same form as Eq. (2) for the quadrupole since $\mathcal{R}(\mu)/R=1+O(\mu^2)$. If not stated otherwise, we consider the eccentricity ε to be the deformation parameter and adapt μ according to Eq. (5).

III. FREQUENCY SPLITTINGS IN DEFORMED MICRODISKS: FULL NUMERICS

Maxwell's equations are solved in two dimensions with Sommerfeld outgoing wave conditions at infinity. The optical modes $\psi(x,y)$ are defined as the solutions with time dependence $e^{-i\omega t}$ where ω is the complex-valued resonant frequency. For convenience, we introduce the dimensionless frequency $\omega R/c=kR$, where c is the speed of light in vacuum

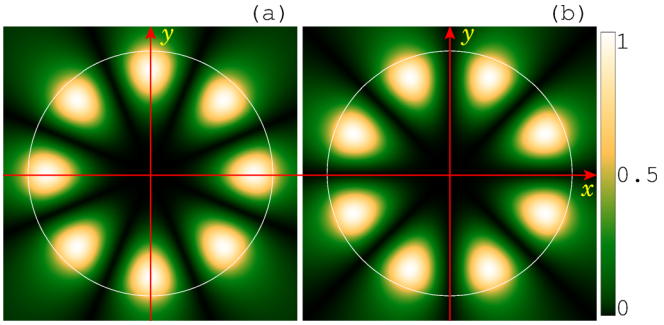

FIG. 1. Intensity patterns of degenerate mode pair $(l,m) = (1,4)$ in the microdisk. Parities are (a) $(\eta_x,\eta_y) = (1,1)$ and (b) $(-1,-1)$. Horizontal and vertical lines are the x and y axes, respectively. Circles mark the cavity boundary. The maximum intensity is normalized to be unity.

and $k = \omega/c$ is the complex-valued wave number. The real part of kR is the conventional frequency while the imaginary part corresponds to half of the linewidth (decay rate), $\gamma/2 = -\mathrm{Im}kR$. We focus here on the transverse magnetic (TM) polarization where the wave function $\psi(x,y)$ is related to the z component of the electric field vector. Throughout the paper we set the effective index of refraction to $n_e = 3.4$.

The cavities considered in this paper have a mirror-reflection symmetry with respect to the x and y axes. Therefore, the wave functions $\psi(x,y)$ can be reduced to the first-quadrant wave function $\psi(x \geqslant 0, y \geqslant 0)$ while the second-, the third-, and the fourth-quadrant wave functions are given by parity coefficients η_x and η_y, possessing 1 or -1: $\psi(-x,y) = \eta_x\psi(x,y)$, $\psi(-x,-y) = \eta_x\eta_y\psi(x,y)$, and $\psi(x,-y) = \eta_y\psi(x,y)$. For instance, Fig. 1 shows the degenerated pair $\{(1,1),(-1,-1)\}$ in the circular cavity with $(l,m) = (1,4)$. For convenience, we refer to the modes having the parity $\eta_y = 1$ and -1 as the even and odd modes, respectively.

The resonant frequencies of the circular microcavity with radius R can be analytically obtained [38] from

$$S_m(kR) \equiv n_e \frac{J'_m}{J_m}(n_e kR) - \frac{H_m^{(1)'}}{H_m^{(1)}}(kR) = 0, \qquad (6)$$

where J, J', H, and H' are the Bessel function, the derivative of the Bessel function, the Hankel function of the first kind, and the derivative of the Hankel function of the first kind, respectively.

Modes in the deformed cavities are computed numerically using the boundary element method (BEM) [39]. Figures 2(a) and 2(c) show the real and the imaginary parts of the resonant frequencies in the elliptic cavity as a function of the deformation parameter. The pairs $\{(\eta_x,\eta_y) = (1,1),(-1,-1)\}$ and $\{(1,-1),(-1,1)\}$ are degenerated in the limit $\varepsilon \to 0$ of the circular cavity. The corresponding data for the quadrupole cavity is shown in Figs. 3(a) and 3(c). The change of the imaginary part of the frequency, i.e., the increase of the decay rate, as a function of the deformation was studied in Ref. [40]. Here, we are interested in the frequency splitting of mode pairs, or more precisely in the real part of the frequency splitting, i.e., $\mathrm{Re}\,\Delta kR \geqslant 0$. Figures 2(b) and 3(b) show that for increasing ε the frequency splitting increases in most cases monotonically both in the ellipse and in the quadrupole.

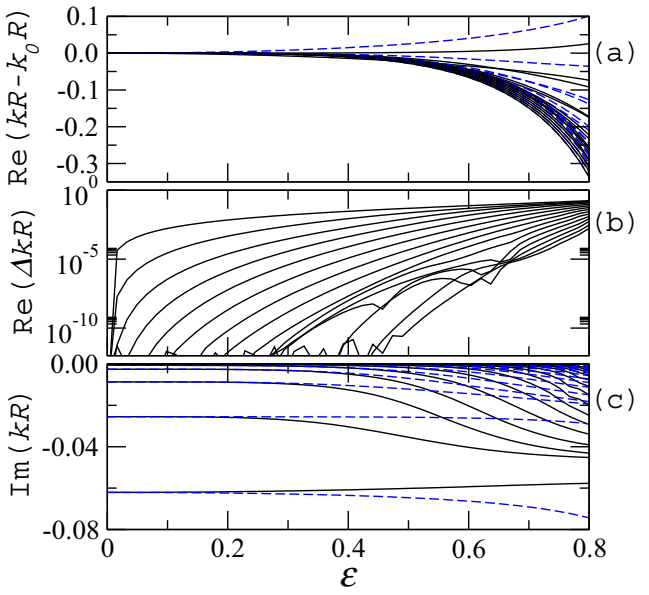

FIG. 2. Resonant frequencies and frequency splittings of mode pairs in the elliptic cavity vs eccentricity ε. Solid and dashed curves in (a) and (c) are for the even $(\eta_y = 1)$ and odd (-1) parities, respectively. (a) Real part of the frequency kR relative to the frequency k_0R of the corresponding mode in the circular cavity. (b) Real part of the frequency splitting of the even and odd modes having the same angular momentum number m as in (a). (c) Imaginary part of the frequency.

For a direct and comprehensive comparison of the two cavities we show in Fig. 4 the frequency splittings of both cavities as a function of the eccentricity and the angular momentum number. The angular momentum number m of the deformed cavity $(\varepsilon \neq 0)$ is chosen according to the corresponding solution in the circular cavity $(\varepsilon = 0)$. In Fig. 4 we can observe that in the low-angular-momentum regime (roughly $m \leqslant 9$),

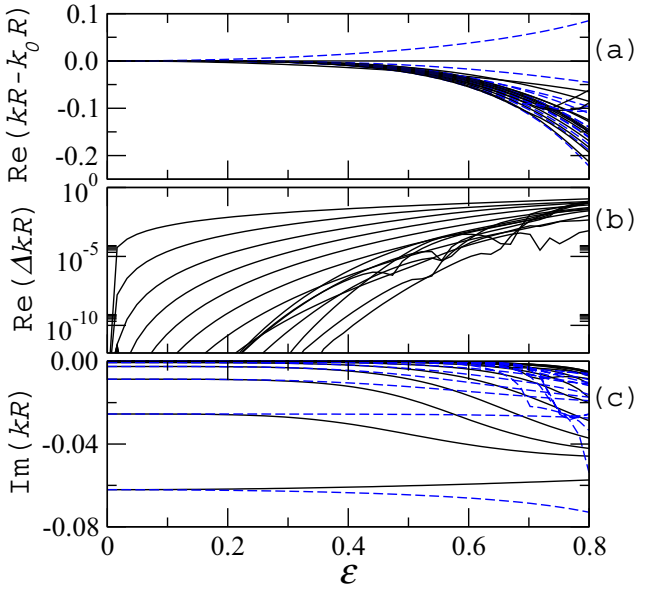

FIG. 3. Same as in Fig. 2 but for the quadrupole cavity.

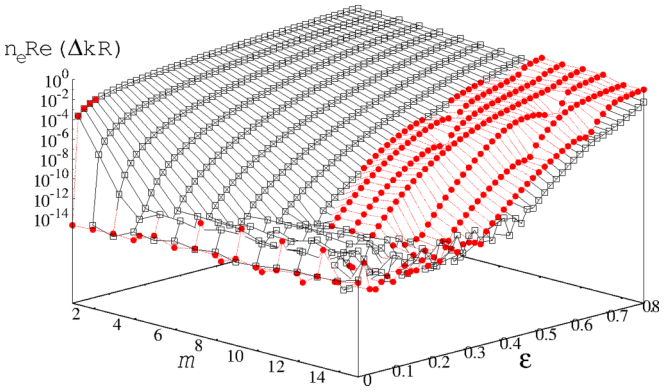

FIG. 4. Frequency splitting of even and odd modes vs eccentricity ε and angular momentum number m. Open squares and solid circles denote the elliptic and quadrupole cavities, respectively. The radial mode number is fixed to $l = 1$. The angular momentum numbers m of the deformed cavities are labeled by those of the corresponding modes in the circular cavity.

the frequency splittings of modes in the elliptic cavity are larger than those of the quadrupole. This order is reversed in the higher-angular-momentum regime. Note that in Fig. 4 two sheets are overlapping as the higher value is eclipsing the other one in order to enhance the visibility of the graph. The cross section of Fig. 4 at $\varepsilon = 0.33$ is plotted in Fig. 5. The flipping of the order in the frequency splitting is more clearly visible.

IV. THE PHASE SPACE OF THE DEFORMED MICRODISKS

In this section we briefly review the well-known phase-space structure of weakly deformed cavities. The short-wavelength limit of wave optics is geometrical (ray) optics. The basic ray model for a microdisk cavity [30] is illustrated in Fig. 6. According to the law of reflection, the incident ray and the reflected ray make the same angle χ with respect to the inward normal vector $\vec{n}$ at the boundary point of the reflection. The ray trajectories (orbits) in real space are mapped into the Poincaré surface of section (SOS) of phase space in the following way. When a ray is reflected at the cavity's boundary, its position in terms of the arclength coordinate along the boundary $s \in [0, L]$ and the tangential component of the normalized momentum $p = \sin\chi \in [-1, 1]$ are recorded. We adopt the convention that $\sin\chi > 0$ means counterclockwise (CCW) propagation and $\sin\chi < 0$ means clockwise (CW) propagation. The coordinates (s, p) are called Birkhoff coordinates.

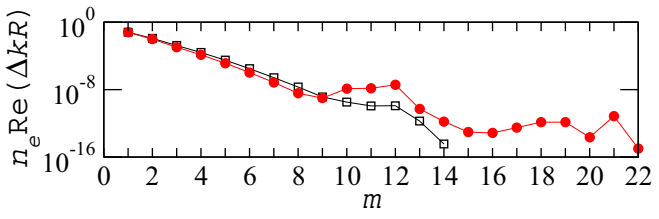

FIG. 5. Frequency splitting as a function of angular momentum m at $\varepsilon = 0.33$; cf. Fig. 4. Open squares and solid circles are splittings in the elliptic and quadrupole cavities, respectively.

The circular cavity is an integrable system and therefore rather special. The angle of incidence, χ, is a constant of motion. Hence, orbits are confined to horizontal lines in the SOS (which in full phase space have the topology of tori); see Fig. 6(b). The ray dynamics on such an invariant torus is in general quasiperiodic and marginally stable. Only on so-called resonant tori the orbits are periodic.

Following the Poincaré-Birkhoff theorem [41], the phase space of a perturbed integrable system exhibits nonlinear resonance chains containing even-numbered isolated stable and unstable periodic orbits which are originated from the destroyed resonant tori. This is illustrated for the elliptic and quadrupole cavity in Figs. 6(c) and 7. For weak deformations, the most prominent resonance chain is related to the so-called bouncing-ball (BB) orbit along the short axis of the cavity. It is a (1:2)-resonance chain; i.e., the stable periodic orbit undergoes two reflections in one period. This resonance chain, which we also call the BB-resonance chain, is located in an intermediate region between the CW zone of $\sin\chi < 0$ and the CCW zone of $\sin\chi > 0$. It enlarges with increasing deformation.

Figures 7(a) and 7(c) compare the phase-space structures of the elliptic and the quadrupole cavities with a small deformation parameter $\varepsilon = 0.05$. Both cavities exhibit almost the same structures, indiscernible by the naked eye. As the deformation is increased [Figs. 7(b) and 7(d)] we can resolve the differences between them, especially the existence of additional resonance chains in the quadrupole cavity. The most prominent ones are the 2(1:3)- and the (1:4)-resonance chain. Here the factor "2" in 2(1:3) means a doubled (1:3) resonance which results in 2×3 stable and unstable fixed points due to the cavity's symmetry; i.e., exhibiting both x- and y-axis symmetry does not allow for odd-numbered resonances.

The tori of CW- (p_-) and CCW-propagating (p_+) rays [see Fig. 6(b)] with the same $|p|$ are degenerated. There is no interaction between them. The waves corresponding to these tori, however, are coupled by the deformation. This coupling leads to a frequency splitting as we discuss in the next sections.

V. PENDULUM APPROXIMATION

An isolated $(t{:}r)$-resonance chain of the weakly deformed cavity [Figs. 6(c) and 7] is accurately approximated by the pendulum Hamiltonian [40,42]

$$H(s,p) = H_0(p) + 2V_{t:r}\cos\left(2\pi r\frac{s}{L} + \phi_0\right), \tag{7}$$

where H_0, $V_{t:r}$, and ϕ_0 are the unperturbed Hamiltonian, the perturbation strength of the $(t{:}r)$ resonance chain, and the global phase, respectively, as illustrated in Fig. 8. The unperturbed Hamiltonian corresponding to the phase space of the circular cavity is given by [40]

$$H_0(p) = 2\left(p\arccos(p) - \sqrt{1-p^2} + \sqrt{1-p_{t:r}^2}\right) - \omega_{t:r}\,p, \tag{8}$$

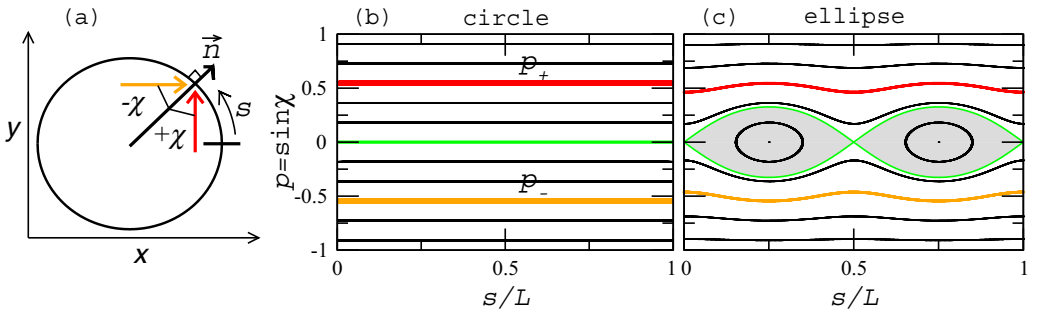

FIG. 6. (a) Real-space illustration of ray dynamics in a two-dimensional cavity. $\pm\chi$ are the incident angles of rays with respect to the normal vector $\vec{n}$ on the cavity boundary. Positive and negative signs indicate counterclockwise and clockwise propagation, respectively. Poincaré surface of section for the (b) circular (eccentricity $\varepsilon = 0$) and (c) elliptic ($\varepsilon = 0.33$) cavities. The horizontal axis is the arclength s normalized by the cavity perimeter L; $s = 0$ corresponds to polar angle $\phi = 0$. The vertical axis is the tangential component of the unit momentum of a ray colliding with the cavity boundary with incident angle χ. Designated $p_\pm$ in (b) are the tori having the same $|p| = \sin|\chi|$ with opposite signs of χ.

where $\omega_{t:r} \equiv 2\arccos(p_{t:r})$ and $p_{t:r} = \cos(t\pi/r)$. An expansion of H_0 in Eq. (8) around $p_{t:r}$ is given by [40]

$$H_0(p) \approx -\frac{(p-p_{t:r})^2}{\sqrt{1-p_{t:r}^2}} + O[(p-p_{t:r})^3]. \tag{9}$$

The perturbation strength $V_{t:r}$ in Hamiltonian (7) is calculated by the area of the $(t:r)$-resonance chain in phase space. To this end, we first obtain the separatrix p_u bounding the $(t:r)$-resonance chain, with the global phase of our system $\phi_0 = \pi$, as follows:

$$-2V_{t:r} = -\frac{(p_u - p_{t:r})^2}{\sqrt{1-p_{t:r}^2}} - 2V_{t:r}\cos\left(2\pi r\frac{s}{L}\right), \tag{10}$$

$$\begin{aligned} p_u &= p_{t:r} \pm \sqrt{2V_{t:r}\left[1-\cos\left(2\pi r\frac{s}{L}\right)\right]\sqrt{1-p_{t:r}^2}} \\ &= p_{t:r} \pm \sqrt{4V_{t:r}}\sqrt[4]{1-p_{t:r}^2}\,\sin\left(\pi r\frac{s}{L}\right). \end{aligned} \tag{11}$$

Integration of the separatrix in Eq. (11) with respect to s for fixed ε (see Fig. 8) gives the ε-dependent phase-space area of the resonance chain:

$$\begin{aligned} \mathcal{A}_{t:r}(\varepsilon) &= \int_0^L p_u^+ ds - \int_0^L p_u^- ds \\ &= 2r\sqrt{4V_{t:r}}\sqrt[4]{1-p_{t:r}^2}\int_0^{L/r}\sin\left(\pi r\frac{s}{L}\right)ds \\ &= \frac{4L\sqrt{4V_{t:r}}}{\pi}\sqrt[4]{1-p_{t:r}^2}. \end{aligned} \tag{12}$$

From Eq. (12) we get the perturbation strength:

$$V_{t:r}(\varepsilon) = \left(\frac{2\pi}{L}\right)^2 \frac{\mathcal{A}_{t:r}(\varepsilon)^2}{256\sqrt{1-p_{t:r}^2}}. \tag{13}$$

We first determine the coupling strength between CW- and CCW-propagating waves induced by the (1:2)-resonance chain and so we use $p_{1:2} = 0$, leading to $V_{1:2}(\varepsilon) = \mathcal{A}_{1:2}(\varepsilon)^2(2\pi/L)^2/256$. In calculating the area of the (1:2) resonance chain, we employ the adiabatic invariant curve $p_a(s) \equiv \sqrt{1-\beta\kappa^{2/3}(s)}$ [37,43]. This curve is characterized by a constant β and the local curvature $\kappa(s)$ of the cavity

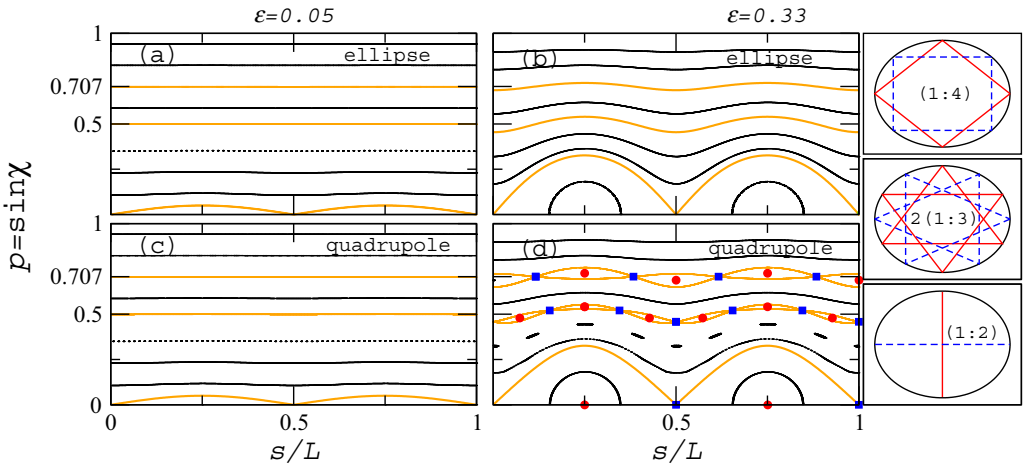

FIG. 7. Poincaré surface of section of the elliptic and quadrupole cavities. Because of symmetry, only the $p \geqslant 0$ region is shown. (a) Elliptic and (c) quadrupole cavity at $\varepsilon = 0.05$. (b) Elliptic and (d) quadrupole cavity at $\varepsilon = 0.33$. Thick curves around $p = 0.5$ and 0.707 are tori related to the 2(1:3) and (1:4) periodic orbits. Real-space geometries of the stable (solid lines) and unstable (dashed lines) periodic orbits in (d) are illustrated on the right-hand side.

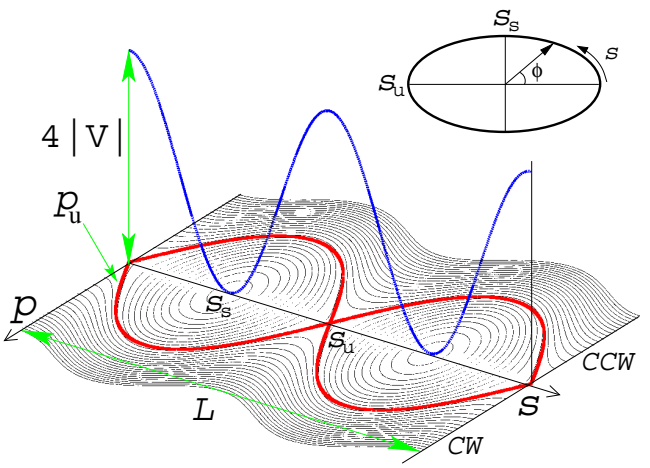

FIG. 8. Schematic diagram of the phase space generated by Hamiltonian (7) with $(t:r) = (1:2)$. L, $s_{s(u)}$, and p_u are, respectively, the perimeter of the cavity, the arclength corresponding to the stable (unstable) periodic orbit, and the momentum corresponding to the separatrix, the curve separating the interior and the exterior of the resonance chain.

boundary. The constant β of the (1:2)-resonance chain can be obtained by

$$p_a(s_u) = \sqrt{1-\beta_u \kappa^{2/3}(s_u)} = 0,$$
$$\beta_u = \kappa^{-2/3}(s_u),$$

where $s_u = 0$ or $L/2$ are the highest curvature points on the cavity boundary; see Fig. 8. The area enclosed by this adiabatic invariant curve characterized by β_u is

$$\mathcal{A}_{1:2} = \oint p_a(s)ds = 2\int_0^{2\pi} \sqrt{[1-\beta_u\kappa^{2/3}(\phi)][\rho^2(\phi)+\dot{\rho}^2(\phi)]}d\phi, \quad (14)$$

with the cavity boundary $\rho(\phi)$ and its derivative $\dot{\rho}(\phi) = d\rho/d\phi$. Using the curvature expressed in the polar coordinate ϕ [37], Eq. (13) is expressed as an integral with respect to ϕ along the given boundary $\rho(\phi)$,

$$V_{1:2} = \left(\frac{2\pi}{L}\right)^2 \frac{1}{64}\left\{\int_0^{2\pi} d\phi\sqrt{\rho^2(\phi)+\dot{\rho}^2(\phi)}\right.$$
$$\left.\overline{-\beta_u[\rho^2(\phi)+2\dot{\rho}^2(\phi)-\rho(\phi)\ddot{\rho}(\phi)]^{2/3}}\right\}^2, \quad (15)$$

with the cavity boundaries in Eqs. (2) and (3).

Figure 9 shows the perturbation strength $V_{1:2}(\varepsilon)$ for the elliptic and the quadrupole cavities calculated using Eq. (15). As expected from Eq. (4) and Figs. 7(a) and 7(c) for weak deformation the perturbation strengths are almost identical. For higher deformation, however, they deviate; see, e.g., the inset in Fig. 9. In fact even for weak deformation, the perturbation strength of the elliptic cavity is slightly larger than that of the quadrupole cavity and this explains the larger frequency splittings in the elliptic cavity in the low-angular-momentum-number regime (Figs. 4 and 5).

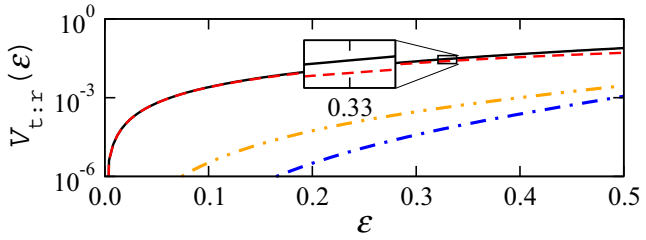

FIG. 9. Perturbation strength $V_{t:r}$ vs deformation parameter ε. The solid (dashed) curve corresponds to the (1:2)-resonance chain in the elliptic (quadrupole) cavity calculated from Eq. (15). The dot-dashed and the dot-dot-dashed curves correspond to the 2(1:3)- and (1:4)-resonance chains in the quadrupole cavity calculated from Eq. (16). Inset: magnification around $\varepsilon = 0.33$.

The perturbation strength $V_{t:r}(\varepsilon)$ for the additional $(t:r)$-resonance chains in the quadrupole cavity can be determined by evaluating the trace of the monodromy matrix $M_{t:r}$ of the stable periodic orbit [44]:

$$V_{t:r} = \left(\frac{L}{2\pi}\right)^2 \frac{\sqrt{1-p_{t:r}^2}}{4r^4}\left\{\arccos\left[\frac{\mathrm{Tr}\, M_{t:r}}{2}\right]\right\}^2. \quad (16)$$

This simpler approach is here accurate enough since the area of such an additional resonance chain is much smaller than that of the BB-resonance chain. Figure 9 shows $V_{t:r}(\varepsilon)$ for the 2(1:3)- and (1:4)-resonance chains.

VI. RESONANCE-ASSISTED TUNNELING

We use the pendulum approximation of the BB-resonance chain to predict the frequency splitting between even- and odd-parity modes in the deformed cavities. We recall that the splitting ΔE_m of the mth degenerated eigenstate pair in the quantum pendulum

$$H(\hat{p},\hat{\theta}) = \frac{\hat{p}^2}{2} + 2V\cos(2\hat{\theta}) \quad (17)$$

was derived in Refs. [45,46] as

$$\Delta E_m = 2V \prod_{\substack{u=-(m-2) \\ \Delta u=2}}^{(m-2)} \frac{V}{E_m - E_u}. \quad (18)$$

In this equation u takes the values $u = -(m-2), -(m-4), \ldots, (m-4), (m-2)$ because of the perturbation proportional to $\cos(2\theta)$. In order to adapt this result to a cavity with a resonance chain described by Hamiltonian (7) we need to figure out the connection between ΔE_m and $\mathrm{Re}(\Delta k_m R)$. From Eq. (9) we identify the energies of the circular (unperturbed) cavity through the semiclassical relation $p_m = m/n_e \mathrm{Re}(k_m R)$ [37], which gives

$$E_m \equiv H_0(p_m) = \hbar_m^2 \mathcal{M}_m^2 \quad (19)$$

with effective Planck constant $\hbar_m \equiv 1/n_e \mathrm{Re}(k_m R)$, $\mathcal{M}_m^2 \equiv -(m-m_{t:r})^2/\sqrt{1-p_{t:r}^2}$, and $m_{t:r} \equiv n_e \mathrm{Re}(k_m R) p_{t:r}$. Equation (19) is the analog to the relation $E_m \propto \hbar^2 m^2$ of the original quantum pendulum but with an m-dependent Planck constant. The differentiation of Eq. (19), $dE_m = 2\hbar_m \mathcal{M}_m^2 d\hbar_m$, results

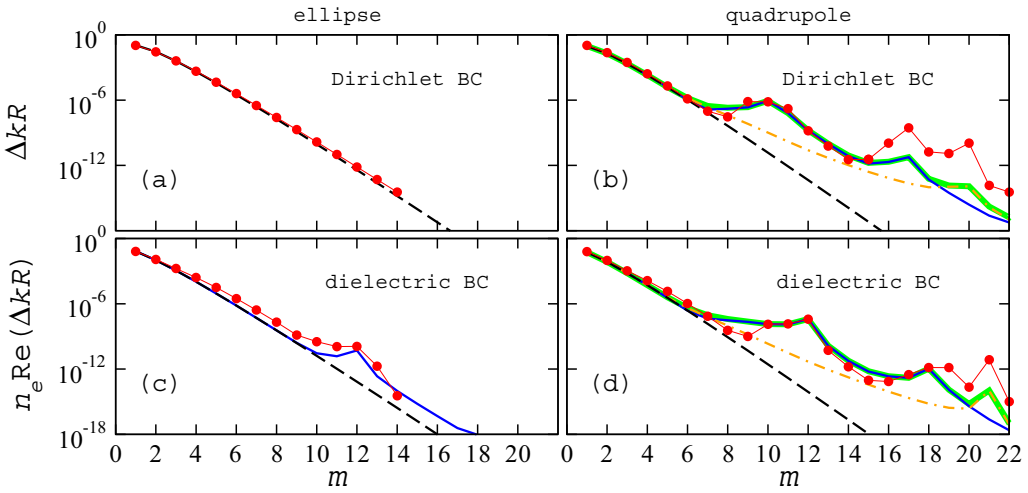

FIG. 10. Frequency splitting of mode pairs as a function of the angular momentum number m at $\varepsilon = 0.33$. (a) Closed ellipse with Dirichlet boundary conditions (BC), (b) closed quadrupole, (c) dielectric ellipse, and (d) dielectric quadrupole. Solid circles with thin lines are full numerical (BEM) calculations. Dashed, thin solid, and dot-dashed curves are results of Eq. (25) of the individual (1:2), (1:2) + 2(1:3), and (1:2) + (1:4) resonance chain contributions, respectively. Thick solid curves in (b) and (d) are combined (1:2) + 2(1:3) + (1:4) resonance chain contributions.

in (with assumption $dX \approx \Delta X$)

$$\frac{\Delta E_m}{E_m} = 2\frac{\mathrm{Re}(\Delta k_m R)}{\mathrm{Re}(k_m R)}, \tag{20}$$

where ΔE_m and $\mathrm{Re}(\Delta k_m R)$ are defined to be positive. Then inserting Eq. (20) into Eq. (18) with $V = V_{1:2}$ yields

$$\mathrm{Re}(\Delta k_m R) = \mathrm{Re}(k_m R)\frac{V_{1:2}}{E_m}\prod_{\substack{u=-(m-2)\\ \Delta u=2}}^{(m-2)} \frac{V_{1:2}/\hbar_m^2}{E_m/\hbar_m^2 - E_u/\hbar_u^2}. \tag{21}$$

All energies in Eq. (21) are scaled because each energy $E_m = \hbar_m^2 \mathcal{M}_m^2$ takes a different $\hbar_m$ in Eq. (19). Hence, one needs to rescale each of the terms with the corresponding $\hbar_m^2$ in order to make them comparable in the Hamiltonian in Eq. (7). Note that despite that this rescaling is crucial for the terms in the product part, the significance of it diminishes when $\hbar$ in the numerator and the denominator are the same (i.e., when $k_m \approx k_u$) and can be factored out.

Equation (21) can be further simplified by the assumption that the mode, having large angular momentum number $m \gg 1$, is a well-confined whispering-gallery mode; i.e., $\mathrm{Re}(k_m R) \gg 1$ and $|\mathrm{Im}(k_m R)| \ll \mathrm{Re}(k_m R)$. In this case the asymptotic relation $m \approx n_e \mathrm{Re}(k_m R)$ [38,47] holds and can be used to remove the denominator term of the prefactor in Eq. (21) as $|E_m| \to 1$ in Eq. (19) with $p_{1:2} = 0$. Therefore, we arrive at the final prediction of the frequency splitting induced by the BB-resonance chain:

$$\begin{aligned} &n_e \mathrm{Re}(\Delta k_m R)_{\mathrm{BB}} \\ &\quad = n_e \mathrm{Re}(k_m R) V_{1:2} \\ &\qquad \times \prod_{\substack{u=-(m-2)\\ \Delta u=2}}^{(m-2)} \frac{V_{1:2}[\mathrm{Re}(k_m)]^2}{H_0(p_m)[\mathrm{Re}(k_m)]^2 - H_0(p_u)[\mathrm{Re}(k_u)]^2}. \end{aligned} \tag{22}$$

Note that in Eq. (19) of Ref. [40] a similar product was given without the scaling with $\hbar_m$ because $\mathrm{Re}(k_m R)$ of the mode $(l,m)=(1,m)$ is compared to $\mathrm{Re}(k_u R)$ of the mode $(1+t, m-r)$, which are very similar near the RAT peak in the decay rate. However, in our case [Eq. (22)] $\mathrm{Re}(k_m R)$ and $\mathrm{Re}(k_u R)$ are quite different since both belong to the same radial mode number $l = 1$ but different angular momentum numbers m and u; i.e., $\mathrm{Re}(k_u R) < \mathrm{Re}(k_m R)$ for $u < m$. Thus, the scaling cannot be neglected in Eq. (22).

It is instructive to mention that the coupling of the perturbation $\sim \cos(n\theta)$ only occurs when $2m \mod n = 0$ (not shown here). For example, when $n = 3$ as in Ref. [48], the coupling can give rise to the frequency splitting only for $m = 3, 6, 9, \ldots$.

Before proceeding to the main results of the dielectric cavities, we first calculate the frequency splittings of Eq. (22) in the closed cavities satisfying the Dirichlet boundary condition on the cavity boundary. Figure 10(a) shows excellent agreement between the numerical results of the BEM and Eq. (22) for the elliptic cavity. However, in the quadrupole cavity in Fig. 10(b), this agreement breaks down above $m = 8$ where several spikes are present in the full numerical result. It is here worth mentioning that frequency splittings in the closed cavities were discussed in Ref. [49] through a perturbative scattering matrix approach. However, the work in Ref. [49] did not address the semiclassical origin of the coupling strength; rather they carried out the decomposition of the scattering matrix to obtain the coupling strength located in the off-diagonal components of the scattering matrix.

Figures 10(c) and 10(d) demonstrate that there are two major differences between the closed and the dielectric cavities. The first difference is the spike structure around $m = 12$, which is absent in the closed elliptic cavity. The other difference is that the spike position of the frequency splittings in the dielectric quadrupole is shifted to higher values of m compared to that of the closed quadrupole. The role of the different boundary conditions is more deeply analyzed in the following.

VII. ADDITIONAL RESONANCE CHAINS CONTRIBUTING TO RAT

In this section we demonstrate that the spikes [Figs. 10(b)–10(d)] in the higher-angular-momentum regime are consequences of the tunneling enhancement due to additional resonance chains as shown in Fig. 7(d). We determine the coupling strength of such an additional $(t{:}r)$-resonance chain by evaluating the trace of the monodromy matrix $M_{t:r}$ of the stable periodic orbit [Eq. (16)]. Note that the additional $(t{:}r)$-resonance chains are located outside of the BB-resonance chain and below the momentum $p_{l,m}$ of the considered mode.

In the same spirit as in Refs. [40] we can determine the enhancement of the splittings via the RAT of an additional $(t{:}r)$-resonance chain. We know that the unperturbed modes $|l,m\rangle_0$ and $|l+it,m-ir\rangle_0$, $i=1,2,\ldots$, can couple through the $(t{:}r)$ resonance, obeying a selection rule in accordance with the Fermi resonance relation [50]. So, the coupled mode $|l,m\rangle$ can be expanded as

$$|l,m\rangle = |l,m\rangle_0 + \sum_{i=1}^{\mathcal{N}_{t:r}} a_i^{t:r} |l+it,m-ir\rangle_0, \tag{23}$$

where the expansion coefficients are given by the secular perturbation theory [11,12] as

$$a_i^{t:r} = \prod_{j\leqslant i} \frac{V_{t:r}[\mathrm{Re}(k_{l,m})]^2}{H_0(p_{l,m})[\mathrm{Re}(k_{l,m})]^2 - H_0(p_{l+jt,m-jr})[\mathrm{Re}(k_{l+jt,m-jr})]^2}, \tag{24}$$

where $\mathcal{N}_{t:r} < [m/r]$. Here $[\cdot]$ denotes an integer part of the argument. Then, since the tunneling rate can be assumed to be additive [12], straightforwardly, the coupling strength, i.e., the splitting, is also additive. Hence, the splitting of the mode in Eq. (23) is enhanced by the sum of the individual contributions of the entire coupled modes. To make it more lucid, it is helpful to see the one-to-one correspondence between Ref. [12] and our work: $|m\rangle_0 \mapsto |l,m\rangle_0$, $|\psi_{\mathrm{ch}}\rangle \mapsto |l,-m\rangle_0$, $\gamma_m^d \mapsto n_e \mathrm{Re}(\Delta k_{l,m} R)_{\mathrm{BB}}$, and $\gamma_m \mapsto n_e \mathrm{Re}(\Delta k_{l,m} R)$. Lastly, since we consider not only a single resonance $(t{:}r)$, our prediction for the frequency splitting has the final form

$$n_e \mathrm{Re}(\Delta k_{l,m} R) = n_e \mathrm{Re}(\Delta k_{l,m} R)_{\mathrm{BB}} + n_e \sum_{\{t:r\}} \sum_{i=1}^{\mathcal{N}_{t:r}} \left|a_i^{t:r}\right|^2 \mathrm{Re}(\Delta k_{l+it,m-ir} R)_{\mathrm{BB}}. \tag{25}$$

In order to implement Eq. (25), we examine the phase space of the quadrupole cavity in Fig. 7(d) and find two prominent resonance chains $(t{:}r) = 2(1{:}3)$ and $(1{:}4)$ at $p_{2(1:3)} \approx 0.5$ and $p_{1:4} \approx 0.707$.

A. Goos-Hänchen shift as an extra perturbation

For the dielectric cavities the influence of the dielectric boundary condition has to be included into the semiclassical description. This is here done in terms of the Goos-Hänchen shift (GHS) [51–53]. The GHS is a spatial lateral shift of a beam upon reflection at a dielectric interface. Its origin is interference of the partial waves which accumulate different phases for the given incident angles.

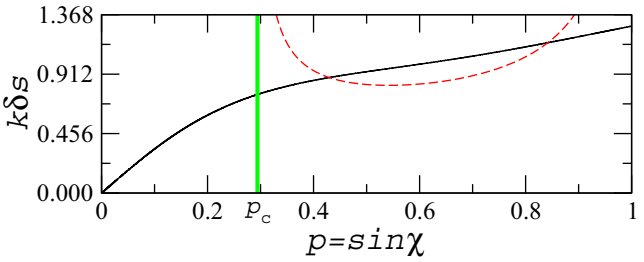

FIG. 11. Goos-Hänchen shift δs vs $p = \sin\chi$. Solid and dashed curves are the numerical results using the scheme of Ref. [51] and the approximated result in Eq. (26); $kR = 4.56$. The thick vertical line at $p_c = 1/n_e = 0.294$ marks the critical line of total internal reflection.

The GHS shows up here in two ways. First, when included as a wave correction into the ray dynamics ("extended ray dynamics") it acts as the extra perturbation (beside the boundary deformation) [54]. As is well known, the integrable ray dynamics in the ellipse (without GHS) does not possess resonance chains except for the (1:2)-resonance chain [55]. In the extended ray dynamics in the ellipse, however, additional resonance chains appear [54]. The extended ray dynamics is carried out here by using the numerical scheme of Ref. [51] for the GHS at a planar interface. This scheme is more accurate than the approximation well above the critical line [56]:

$$\delta s = \frac{2}{k} \frac{p}{\sqrt{(n_e^2 p^2 - 1)(1-p^2)}}. \tag{26}$$

Figure 11 shows the numerical result using the scheme of Ref. [51] in comparison with approximation (26). It is obvious that the singularities at $n_e^2 p^2 = 1$ and $p = 1$ in Eq. (26) should be considered carefully; however, the resonances addressed in the present paper, $p_{1:4} = 0.707$ and $p_{2(1:3)} = 0.5$, are located far from both singularities $p = 1/n_e = 0.294$ and $p = 1$.

Figure 12 shows the phase space of the extended ray dynamics in the ellipse at $\varepsilon = 0.33$. The new 2(1:3)-resonance chain originated from the (1:3)-resonant torus which is destroyed by the GHS. The coupling strength, based on the trace of the monodromy matrix of the stable periodic orbit in this resonance chain [Eq. (16)], is obtained as $V_{\mathrm{GHS}^e}^{2(1:3)} =$

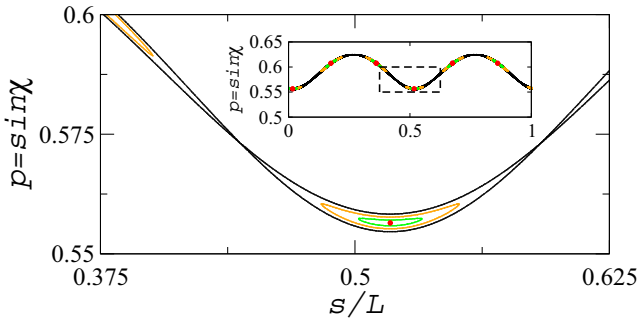

FIG. 12. Small 2(1:3)-resonance chain in the phase space of the elliptic cavity ($\varepsilon = 0.33$) due to the GHS; $kR = 4.56$. The stable periodic orbit is marked by the solid circles.

1.367×10^{-6}. This coupling is much smaller than the coupling induced by the boundary deformation of the quadrupole cavity with the same deformation parameter. For example, the coupling strength of the 2(1:3)-resonance chain of the quadrupole cavity is larger than that of the elliptic cavity as $V_q^{2(1:3)} = 6.5 \times 10^{-5} \gg V_{\mathrm{GHS}^e}^{2(1:3)}$ at $\varepsilon = 0.33$. Hence, the order of the frequency splitting (Figs. 4 and 5) can flip when the enhancement of the RAT process becomes sufficiently strong.

B. Periodic orbit shift induced by GHS

The second important effect of the GHS is the effective momentum shift of the periodic orbits [51]

$$\delta p = \frac{\kappa \delta s}{2}\sqrt{1-p^2}, \tag{27}$$

where κ is the local curvature of the cavity's boundary averaged over the bounce points of the periodic orbit. This effect is automatically included in the extended ray dynamics as the periodic orbits reorganize dynamically. However, when the conventional momentum is used in the RAT formalism, the periodic orbit shift (27) has to be included as a correction [23].

The BB-resonance chain ($p_{1:2} = 0$; see the solid curve in Fig. 11) does not exhibit a GHS. Hence, in Eq. (22) the conventional momentum $p_u = u/n_e \mathrm{Re}(kR)$ [43] for the BB-resonance chain is used.

For the additional resonance chains above the critical line the periodic orbit shift (27) is nonzero. Here, approximation (26) for the GHS is accurate enough. The periodic orbit shift translates into an angular-momentum-number shift

$$\delta m_{t:r} = 1/\sqrt{1-(p_{t:r}n_e)^{-2}} \tag{28}$$

with average radius of curvature $1/\kappa \approx R$. Equation (28) is inserted into Eq. (8) via [40]

$$p_{l,m} = \frac{1}{n_e k_{l,m} R}(m - \delta m_{t:r}). \tag{29}$$

C. RAT in a dielectric microcavity with GHS

The results of Eq. (25) with Ref. [51] and Eq. (29) are plotted in Figs. 10(b)–10(d) by thin solid and dot-dashed curves for 2(1:3)- and (1:4)-resonance chains, respectively. Thick solid curves in Figs. 10(b) and 10(d) are combined results reflecting both resonance chain contributions. For the thin solid curve in Fig. 10(c), we use the coupling strength $V_{\mathrm{GHS}^e}^{2(1:3)}$ obtained before. By comparing the closed and the dielectric quadrupole cavities, we can confirm that in both cases the results of Eq. (25) supported by $a_1^{2(1:3)}$ agree nicely with the full numerical results. However, in the case of RAT supported by $a_2^{2(1:3)}$ and $a_1^{1:4}$, resonance chains fail to reach the exact numerical values. We speculate that this deviation is related to contributions of further additional resonance chains.

The higher m positions of the RAT spikes of the dielectric quadrupole cavity compared to the closed cavity are reproduced successfully by Eq. (25) with the correction in Eq. (29). Also, in Fig. 10(c) we can see the RAT spike of the dielectric elliptic cavity caused by 2(1:3) resonant torus by using $V_{\mathrm{GHS}^e}^{2(1:3)}$. Hence, we accomplished the semiclassical description of frequency splittings in the weakly deformed microcavity via multiple RAT processes incorporating GHS originated from the dielectric boundary condition.

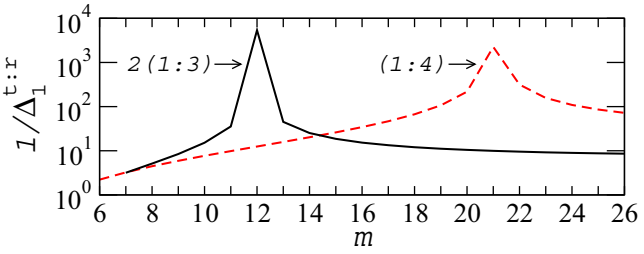

FIG. 13. Degree of degeneracy of Eq. (30) as a function of the angular momentum number m.

D. Degeneracy versus coupling strength

The coupling coefficient $|a_i^{t:r}|^2$ in Eqs. (25) and (24) is determined by both the coupling strength $V_{t:r}$ in the numerator and the degeneracy between the modes in the denominator. It means that a large $(t:r)$-resonance chain can be compensated by a weak degree of degeneracy between $H_0(p_{l,m})[\mathrm{Re}(k_{l,m})]^2$ and $H_0(p_{l+jt,m-jr})[\mathrm{Re}(k_{l+jt,m-jr})]^2$. The case is already observed in Figs. 9 and 10. While the coupling strength of the (1:4)-resonance chain is larger than that of the 2(1:3)-resonance chain in Fig. 9, RAT caused by the 2(1:3)-resonance chain is larger than that of the (1:4)-resonance chain in Fig. 10. The reason is the smaller denominator in Eq. (24) for the 2(1:3)-resonance chain in that angular-momentum-number regime and for the chosen refractive index. Note that this scenario applies not only to the quadrupole cavity but also to the elliptic cavity when the extended ray dynamics is considered.

In order to examine the denominator impact on the contribution coefficient of RAT in Eq. (24), we define the degree of degeneracy as

$$\frac{1}{\Delta_1^{t:r}} \equiv \left|\frac{a_1^{t:r}}{V_{t:r}[\mathrm{Re}(k_{l,m})]^2}\right|. \tag{30}$$

In Fig. 13 it can be seen that the degree of the degeneracy has peaks exactly at the same positions as the spikes in Fig. 10: first $m = 12$ and second $m = 21$ for the 2(1:3)- and (1:4)-resonance chains, respectively. Therefore, the positions of the enhancement of RAT are governed by the degeneracy of H_0 which is independent of $V_{t:r}$. Moreover, since the RAT with respect to the 2(1:3)-resonance chain, corresponding to the first peak, can start at $m - 6 \geqslant 1$, we predict that the flipping of the order of the frequency splittings between the elliptic cavity and the quadrupole cavity, due to the enhancement of RAT, will occur in $7 \leqslant m \leqslant 12$, consistent with the numerical finding in Fig. 5.

E. Husimi function

To further support our conclusions, we investigate the modes in phase space in terms of the Husimi function $h(s,p)$ [57]. Figures 14(a) and 14(b) show as examples the Husimi functions of the modes $(l,m) = (1,12)$ and $(3,6)$ in the quadrupole cavity with $\varepsilon = 0.33$.

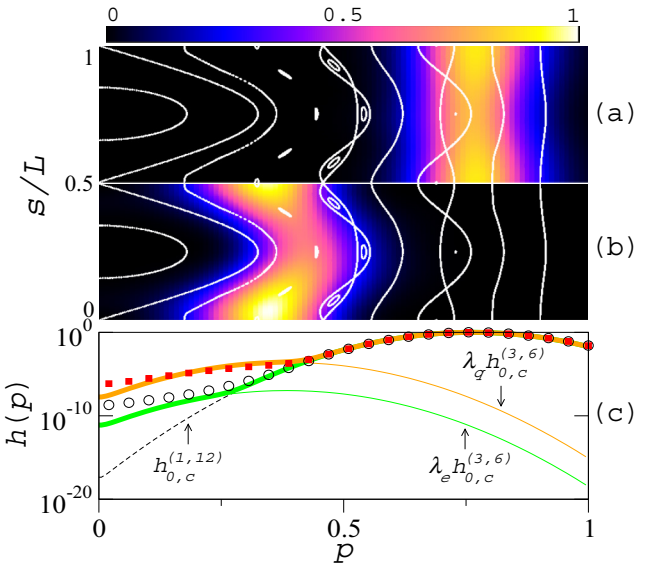

FIG. 14. Husimi functions of the modes (a) $(l,m) = (1,12)$ and (b) (3,6) superimposed on the SOS in the quadrupole cavity with $\varepsilon = 0.33$. In (c), solid squares and open circles are $h^{(1,12)}_{0.33,q}$ and $h^{(1,12)}_{0.33,e}$ and upper and lower thick solid curves are $\xi^{(1,12)}_{0.33,q}$ and $\xi^{(1,12)}_{0.33,e}$, respectively. The maximum intensity is normalized to be unity.

Since the RAT in the present work occurs in the momentum direction, the Husimi functions of the modes (l,m) at fixed deformation parameter ε are projected onto the p axis,

$$h^{(l,m)}_{\varepsilon,j}(p) \equiv \int_0^L h^{(l,m)}_{\varepsilon,j}(s,p)ds, \tag{31}$$

where $j = c$, e, or q for the circle, the ellipse, or the quadrupole. These projected Husimi functions contain information about the mode coupling. In particular, they reflect the coupling coefficient $|a_i^{t,r}|^2$ in Eq. (25). We demonstrate this fact by adding the circular cavity's Husimi functions corresponding to the deformed cavity's modes. As an example, for the mode (1,12) exhibiting RAT with the aid of the 2(1:3)-resonance chain, it gives

$$\xi^{(1,12)}_{0.33,j}(p) = h^{(1,12)}_{0,c}(p) + \lambda_j h^{(3,6)}_{0,c}(p) \tag{32}$$

with

$$\lambda_j \equiv \left|a_1^{2(1:3)}\right|^2_j. \tag{33}$$

The results are plotted in Fig. 14(c) for the quadrupole and the elliptic cavities by the upper and the lower thick solid curves. The coupling coefficients are obtained as $|a_1^{2(1:3)}|^2_q = 2.389 \times 10^{-4}$ and $|a_1^{2(1:3)}|^2_e = 1.052 \times 10^{-7}$ for the quadrupole cavity and the elliptic cavity, respectively. We observe a nice agreement of Eq. (32) and the exact Husimi function in Fig. 14(c). This confirms that the contributions related to the RAT spikes around $m = 12$ in Figs. 10(c) and 10(d) originate from the 2(1:3)-resonance chain.

VIII. SUMMARY

We investigated the frequency splittings in weakly deformed microdisk cavities by means of full numerics and a semiclassical approach based on resonance-assisted tunneling. As examples, an ellipse and a quadrupole shape have been chosen. The ellipse (quadrupole) represents a well-known model of an integrable (nonintegrable) system. In the regime of small angular momentum numbers the frequency splittings in the elliptic cavity are slightly larger than those in the quadrupole cavity. This is traced back to the area of the dominant (1:2)-resonance chain in ray dynamical phase space. The area plays the role of the coupling strength between clockwise- and counterclockwise-propagating waves. In the elliptic cavity the area is larger than that in the quadrupole cavity.

In the higher-angular-momentum-number regime the frequency splittings of the quadrupole cavity are larger than those in the elliptic cavity. The origin is the additional 2(1:3)- and (1:4)-resonance chains. Both do not appear in the elliptic cavity without Goos-Hänchen shift. By explicitly taking into account the Goos-Hänchen shift in the extended ray dynamics inside the elliptic cavity, the enhancement of the frequency splittings is explained. We demonstrated that the resonance-assisted tunneling rate of the quadrupole cavity is larger than that of the elliptic cavity triggered by the Goos-Hänchen shift. The conclusions are confirmed by a study of the resonance-assisted tunneling process in terms of Husimi functions.

Our work clearly shows that for the splitting of frequencies of mode pairs the cavity shape matters. Experiments on frequency splittings in deformed microdisk cavities, such as in Ref. [31], have to care about the precise shape of the cavity deformation.

ACKNOWLEDGMENTS

This research was supported financially by the DFG (Project No. WI1986/7-1). In addition, the High-Tech Convergence Technology Development Program (NRF-2014M3C1A3051331) through the National Research Foundation of Korea (NRF) funded by the Ministry of Science, ICT & Future Planning is acknowledged.

[1] M. J. Davis and E. J. Heller, J. Chem. Phys. **75**, 246 (1981).
[2] S. D. Frischat and E. Doron, Phys. Rev. E **57**, 1421 (1998).
[3] N. Mertig, J. Kullig, C. Löbner, A. Bäcker, and R. Ketzmerick, Phys. Rev. E **94**, 062220 (2016).
[4] G. Hackenbroich and J. U. Nöckel, Europhys. Lett. **39**, 371 (1997).
[5] O. Bohigas, S. Tomsovic, and D. Ullmo, Phys. Rep. **223**, 43 (1993).
[6] S. Keshavamurthy, Int. Rev. Phys. Chem. **26**, 521 (2007).
[7] S. Keshavamurthy and P. Schlagheck, *Dynamical Tunneling: Theory and Experiment* (Taylor & Francis, Boca Raton, FL, 2011).

[8] A. Shudo, Y. Hanada, T. Okushima, and K. S. Ikeda, Europhys. Lett. **108**, 50004 (2014).
[9] C.-H. Yi, H.-H. Yu, and C.-M. Kim, Phys. Rev. E **93**, 012201 (2016).
[10] O. Brodier, P. Schlagheck, and D. Ullmo, Phys. Rev. Lett. **87**, 064101 (2001).
[11] O. Brodier, P. Schlagheck, and D. Ullmo, Ann. Phys. (NY) **300**, 88 (2002).
[12] S. Löck, A. Bäcker, R. Ketzmerick, and P. Schlagheck, Phys. Rev. Lett. **104**, 114101 (2010).
[13] F. Fritzsch, A. Bäcker, R. Ketzmerick, and N. Mertig, Phys. Rev. E **95**, 020202 (2017).
[14] S. Tomsovic and D. Ullmo, Phys. Rev. E **50**, 145 (1994).
[15] M.-W. Kim, S. Rim, C.-H. Yi, and C.-M. Kim, Opt. Express **21**, 32508 (2013).
[16] A. Bäcker, R. Ketzmerick, S. Löck, J. Wiersig, and M. Hentschel, Phys. Rev. A **79**, 063804 (2009).
[17] A. Ramamoorthy, R. Akis, J. P. Bird, T. Maemoto, D. K. Ferry, and M. Inoue, Phys. Rev. E **68**, 026221 (2003).
[18] R. Akis, A. Ramamoorthy, D. Ferry, and J. Bird, J. Comput. Electron. **2**, 281 (2003).
[19] S. Shinohara, T. Harayama, T. Fukushima, M. Hentschel, T. Sasaki, and E. E. Narimanov, Phys. Rev. Lett. **104**, 163902 (2010).
[20] J. Yang, S.-B. Lee, S. Moon, S.-Y. Lee, S. W. Kim, T. T. A. Dao, J.-H. Lee, and K. An, Phys. Rev. Lett. **104**, 243601 (2010).
[21] Q. H. Song, L. Ge, B. Redding, and H. Cao, Phys. Rev. Lett. **108**, 243902 (2012).
[22] Q.-F. Yang, X.-F. Jiang, Y.-L. Cui, L. Shao, and Y.-F. Xiao, Phys. Rev. A **88**, 023810 (2013).
[23] H. Kwak, Y. Shin, S. Moon, S.-B. Lee, J. Yang, and K. An, Sci. Rep. **5**, 9010 (2015).
[24] C. Dembowski, H.-D. Gräf, A. Heine, R. Hofferbert, H. Rehfeld, and A. Richter, Phys. Rev. Lett. **84**, 867 (2000).
[25] R. Hofferbert, H. Alt, C. Dembowski, H.-D. Gräf, H. L. Harney, A. Heine, H. Rehfeld, and A. Richter, Phys. Rev. E **71**, 046201 (2005).
[26] A. Bäcker, R. Ketzmerick, S. Löck, M. Robnik, G. Vidmar, R. Höhmann, U. Kuhl, and H.-J. Stöckmann, Phys. Rev. Lett. **100**, 174103 (2008).
[27] S. Gehler, S. Löck, S. Shinohara, A. Bäcker, R. Ketzmerick, U. Kuhl, and H.-J. Stöckmann, Phys. Rev. Lett. **115**, 104101 (2015).
[28] W. K. Hensinger, H. Haffner, A. Browaeys, N. R. Heckenberg, K. Helmerson, C. McKenzie, G. J. Milburn, W. D. Phillips, S. L. Rolston, H. Rubinsztein-Dunlop *et al.*, Nature (London) **412**, 52 (2001).
[29] K. J. Vahala, Nature (London) **424**, 839 (2003).
[30] H. Cao and J. Wiersig, Rev. Mod. Phys. **87**, 61 (2015).
[31] S. K. Kim, S. H. Kim, G. H. Kim, and Y. H. Lee, J. Korean Phys. Soc. **47**, L397 (2005).
[32] A. Daraei, A. Tahraoui, D. Sanvitto, J. A. Timpson, P. Fry, M. Hopkinson, P. S. S. Guimaraes, H. Vinck, D. Whittaker, M. S. Skolnick *et al.*, Appl. Phys. Lett. **88**, 051113 (2006).
[33] H. A. M. Leymann, C. Hopfmann, F. Albert, A. Foerster, M. Khanbekyan, C. Schneider, S. Höfling, A. Forchel, M. Kamp, J. Wiersig *et al.*, Phys. Rev. A **87**, 053819 (2013).
[34] K. Sebald, M. Seyfried, S. Klembt, and C. Kruse, Opt. Express **19**, 19422 (2011).
[35] B. Gayral, J. M. Gérard, B. Legrand, E. Costard, and V. Thierry-Mieg, Appl. Phys. Lett. **72**, 1421 (1998).
[36] J. U. Nöckel and A. D. Stone, Nature (London) **385**, 45 (1997).
[37] J. U. Nöckel, Ph.D. thesis, Yale University, 1997.
[38] R. Dubertrand, E. Bogomolny, N. Djellali, M. Lebental, and C. Schmit, Phys. Rev. A **77**, 013804 (2008).
[39] J. Wiersig, J. Opt. A: Pure Appl. Opt. **5**, 53 (2003).
[40] J. Kullig and J. Wiersig, Phys. Rev. E **94**, 022202 (2016).
[41] A. J. Lichtenberg and M. A. Lieberman, *Regular and Chaotic Dynamics* (Springer, Berlin, 1992).
[42] J. Kullig, C. Löbner, N. Mertig, A. Bäcker, and R. Ketzmerick, Phys. Rev. E **90**, 052906 (2014).
[43] M. Robnik and M. V. Berry, J. Phys. A **18**, 1361 (1985).
[44] S. Löck, Ph.D. thesis, Technische Universität Dresden, Germany, 2009.
[45] S. Keshavamurthy, J. Chem. Phys. **122**, 114109 (2005).
[46] A. A. Stuchebrukhov and R. A. Marcus, J. Chem. Phys. **98**, 8443 (1993).
[47] Á. Elbert, J. Comput. Appl. Math. **133**, 65 (2001).
[48] S. Sunada and T. Harayama, Opt. Express **15**, 16245 (2007).
[49] G. Hackenbroich, E. Narimanov, and A. D. Stone, Phys. Rev. E **57**, R5 (1998).
[50] C.-H. Yi, H.-H. Yu, J.-W. Lee, and C.-M. Kim, Phys. Rev. E **91**, 042903 (2015).
[51] J. Unterhinninghofen and J. Wiersig, Phys. Rev. E **82**, 026202 (2010).
[52] J. Unterhinninghofen, U. Kuhl, J. Wiersig, H.-J. Stöckmann, and M. Hentschel, New J. Phys. **13**, 023013 (2011).
[53] P. Stockschläder, J. Kreismann, and M. Hentschel, Europhys. Lett. **107**, 64001 (2014).
[54] J. Unterhinninghofen, J. Wiersig, and M. Hentschel, Phys. Rev. E **78**, 016201 (2008).
[55] H. Waalkens, J. Wiersig, and H. R. Dullin, Ann. Phys. (NY) **260**, 50 (1997).
[56] K. Artmann, Ann. Phys. (Leipzig) **437**, 87 (1948).
[57] M. Hentschel, H. Schomerus, and R. Schubert, Europhys. Lett. **62**, 636 (2003).